ADVANCED MATERIALS
www.advmat.de

Monolithic All-Perovskite Tandem Solar Cells with Minimized Optical and Energetic Losses

*Kunal Datta, Junke Wang, Dong Zhang, Valerio Zardetto, Willemijn H. M. Remmerswaal, Christ H. L. Weijtens, Martijn M. Wienk, and René A. J. Janssen**

Perovskite-based multijunction solar cells are a potentially cost-effective technology that can help surpass the efficiency limits of single-junction devices. However, both mixed-halide wide-bandgap perovskites and lead-tin narrow-bandgap perovskites suffer from non-radiative recombination due to the formation of bulk traps and interfacial recombination centers which limit the open-circuit voltage of sub-cells and consequently of the integrated tandem. Additionally, the complex optical stack in a multijunction solar cell can lead to losses stemming from parasitic absorption and reflection of incident light which aggravates the current mismatch between sub-cells, thereby limiting the short-circuit current density of the tandem. Here, an integrated all-perovskite tandem solar cell is presented that uses surface passivation strategies to reduce non-radiative recombination at the perovskite-fullerene interfaces, yielding a high open-circuit voltage. By using optically benign transparent electrode and charge-transport layers, absorption in the narrow-bandgap sub-cell is improved, leading to an improvement in current-matching between sub-cells. Collectively, these strategies allow the development of a monolithic tandem solar cell exhibiting a power-conversion efficiency of over 23%.

1. Introduction

Multijunction photovoltaics (PV), pairing multiple absorber layers with cascaded bandgaps, have demonstrated higher power conversion efficiencies (PCEs) than that achievable using single-junction solar cells.[1] Recent advances in metal-halide perovskites with a wide range of bandgaps have motivated their use in tandems with perovskite, crystalline silicon (c-Si), and copper indium gallium selenide (CIGS), among other PV technologies.[2] Of particular interest is the development of all-perovskite tandem solar cells that promise low-cost solution processing and high efficiencies. As a result, in less than a decade, gains made in material discovery and processing have led the PCE of all-perovskite tandems to a certified value of 26.4%, higher than 25.5% for single-junction perovskite solar cells (PSCs) and close to the 26.7% for state-of-the-art c-Si devices.[3]

Device and optical simulations predict that monolithic, all-perovskite tandem solar cells can reach an empirical limit of 33.6% by coupling 1.77/1.22 eV absorbers.[4] For lead halide perovskites, with a nominal ABX_3 crystal composition, the wide-bandgap absorber is typically obtained by mixing Br^- or Cl^- with I^- at the X-site,[5] whereas the narrow bandgap is achieved by alloying Pb^{2+} with Sn^{2+} at the B-site.[6] Closing the efficiency gap requires optimizing the performance of both sub-cells.[7] The wide-bandgap cell typically suffers from a large bandgap to open-circuit voltage (V_{oc}) deficit, originating from non-radiative recombination losses in the perovskite film and at perovskite/charge transport layer heterojunctions.[8,9] Additionally, light-induced halide segregation in I/Br-mixed perovskites raises concerns over their operational stability.[10] Mitigation strategies such as using additives and surface treatments to improve the film quality, and developing new charge transport materials to enable better energy alignment, have been investigated to address such issues encountered in wide-bandgap perovskites.[11–13] On the other hand, the narrow-bandgap cell is limited by a significant short-circuit current density (J_{sc}) loss, as a result of the low absorptivity of Pb—Sn hybrid perovskite in the near-infrared (NIR) region and a reduced charge extraction efficiency during operation.[14,15] Meanwhile, uncontrolled hole doping due to Sn^{2+} oxidation can drastically reduce the carrier diffusion length and impede the use of a thick absorbing layer.[16] Modifying such perovskite films with judiciously selected additives and post-treatments can help increase carrier lifetime and consequently device performance.[15,17–20]

Next to optimizing individual cells at each bandgap, electrical and optical constraints of a tandem configuration must also be considered.[7,21] Sub-cells are electrically and optically connected

K. Datta, J. Wang, D. Zhang, W. H. M. Remmerswaal, C. H. L. Weijtens, M. M. Wienk, R. A. J. Janssen
Molecular Materials and Nanosystems and Institute of Complex Molecular Systems
Eindhoven University of Technology
Partner in Solliance
P.O. Box 513, Eindhoven 5600 MB, The Netherlands
E-mail: r.a.j.janssen@tue.nl
D. Zhang, V. Zardetto
TNO
Partner in Solliance
High Tech Campus 21, Eindhoven 5656 AE, The Netherlands
R. A. J. Janssen
Dutch Institute for Fundamental Energy Research
De Zaale 20, Eindhoven 5612 AJ, The Netherlands
The ORCID identification number(s) for the author(s) of this article can be found under https://doi.org/10.1002/adma.202110053.

DOI: 10.1002/adma.202110053

by an interconnecting layer (ICL) in a two-terminal tandem device.[22] The ICL ensures band alignment for efficient charge collection and ohmic contact for fast recombination while maintaining a good solvent barrier to prevent damage due to solution-processed perovskites and charge-transport layers.[22,23] State-of-the-art ICLs using a fullerene/SnO_2/Au/poly(3,4-ethylene dioxythiophene):polystyrene sulfonate (PEDOT:PSS) stack with low-electrical losses have been reported for efficient all-perovskite multijunction solar cells.[17,24,25] Furthermore, optical losses due to parasitic absorption in the front transparent conductive oxide (TCO), and reflection at the air/glass interface limits the maximum achievable J_{sc} of state-of-the-art tandem solar cells by limiting light exposure and thereby widening the current mismatch between sub-cells.[21] Improving light management techniques can therefore greatly improve the performance of all-perovskite tandem solar cells, as they have done in perovskite-silicon multijunctions.[21,26,27]

Here, we report the development of efficient all-perovskite tandem solar cells enabled by the suppression of non-radiative recombination and optical losses. We begin by describing the passivation of surface defects at the interface of the wide-bandgap perovskite with the electron transport layer using a solution-processed quaternary ammonium halide passivation layer which translates to solar cells with a high V_{oc}. We also find that passivating the surface of narrow-bandgap perovskite film is crucial for obtaining a high V_{oc}. In addition, we use an ultrathin hole transport layer (HTL) to enhance the J_{sc} of the narrow-bandgap device. Finally, by adopting a front TCO with high mobility and low parasitic free-carrier absorption, we fabricate tandem solar cells with minimal losses in the NIR spectral range that narrows the current-mismatch between sub-cells. After optimization, we demonstrate efficient all-perovskite tandem solar cells with a PCE of over 23%.

2. Results and Discussion

Wide-bandgap, mixed-halide perovskite films were prepared using a mixed-cation (formamidinium (FA), methylammonium (MA), potassium (K), and cesium (Cs)) formulation. Briefly, solutions of $FAPbI_3$ and $MAPbBr_3$ were mixed in the required volumetric ratio (3:2) to get the desired halide (iodide:bromide) ratio. CsI was added to this stock solution and KI was added in order to improve the photostability of the thin film.[11] The precursor solution was cast onto a spinning substrate and upon subsequently dropping an antisolvent (anisole), the wet film immediately changed color due to the nucleation of perovskite crystals. With thermal annealing and the loss of residual solvent, the film turned dark, leading to the formation of a polycrystalline film. Surface morphology and X-ray diffractogram show the formation of a high-quality pin-hole free perovskite film with minimal unreacted PbI_2 (Figure S1, Supporting Information). UV–vis-NIR and photoluminescence spectra confirm the optical bandgap of ≈1.77 eV, close to the ideal top-cell bandgap for an all-perovskite multijunction solar cell.[28] The photoluminescence transient of the band-to-band emission shows a mono-exponential decay with a lifetime of ≈220 ns.

The measurement of absolute photoluminescence of thin films has been used to determine the quasi-Fermi level splitting (QFLS) in the presence of charge-transporting interfaces and has helped identify critical losses due to interfacial recombination.[29] **Figure 1**a shows the absolute photoluminescence spectrum of the 1.77 eV perovskite film (w/o C_{60}) deposited on a hole-transporting surface (glass/ITO/HTL) using [2-(9H-carbazol-9-yl)ethyl]phosphonic acid (2PACz) as a self-assembled hole-transporting monolayer. An increase in non-radiative recombination is observed when a thermally evaporated C_{60} electron-transport layer is deposited on top of the perovskite surface (w/ C_{60}), causing a drop in the emitted spectral photon flux density. In contrast, the 2PACz/perovskite interface causes only a marginal decrease compared to perovskite on glass (Figure S2, Supporting Information) of the photon flux, thereby emphasizing the perovskite/C_{60} interface as a key bottleneck in cell development. Upon the application of a solution-processed quaternary ammonium halide salt (choline chloride) at this interface,[30] the absolute photoluminescence spectrum (Figure 1b) of the passivated film overlaps with that of the passivated film coated with C_{60}, indicating a steep reduction in interfacial non-radiative recombination. This is reflected in the QFLS values estimated from these measurements using the high-energy linear-fitting method (Figure 1c). In the absence of surface passivation, a ≈99 mV loss in QFLS is registered upon the introduction of the C_{60} transport layer. This loss reduces to only ≈4 mV in a passivated film. Here, we also find that the loss incurred at the perovskite/C_{60} interface increases with widening the optical bandgap (between 1.63 and 1.77 eV); nevertheless, the surface treatment is also efficacious in other mixed-halide perovskite compositions, pointing to identical interfacial recombination processes dominating performance loss irrespective of perovskite bandgap or halide content (Figure S3, Supporting Information).

Single-junction PSCs (Figure 1d) were subsequently developed in the inverted (*p-i-n*) architecture using 2PACz and C_{60} hole- and electron-selective contacts respectively.[12] The energy level diagram (Figure S4, Supporting Information) comparing the hole-transporting interface of a 1.77 eV PSC shows that self-assembled monolayer (SAM) 2PACz has a better band alignment to the valence band of the perovskite absorber, compared to commonly used polymeric material (poly[bis(4-phenyl)(2,4,6-trimethylphenyl)amine], PTAA), leading to low energetic loss at the hole-transporting interface. The combination of low-loss perovskite/2PACz and choline chloride-passivated perovskite/C_{60} interfaces (Figure 1e,f) yield solar cells with high V_{oc} and stable PCE of ≈15.8%. Here, the passivation provides a V_{oc} gain of ≈60 mV compared to the control cell. The stability under continuous irradiation (Figure 1g) also validates the high threshold of the wide-bandgap absorber against degradation due to light-induced halide segregation. The performance of the cell can be further improved by using a recently-reported [4-(3,6-dimethyl-9H-carbazol-9-yl)butyl]phosphonic acid (Me-4PACz) hole-transport layer that yields a higher fill factor (FF), resulting in a stabilized efficiency of ≈16.7% (Figure S5, Supporting Information).[31] This has been attributed to reduced interfacial trapping at the perovskite/hole-transport layer interface and agrees well with prior observations in perovskite-silicon tandem solar cells.[31,32] However, the noticeably poorer wetting of the perovskite on Me-4PACz compared to on 2PACz

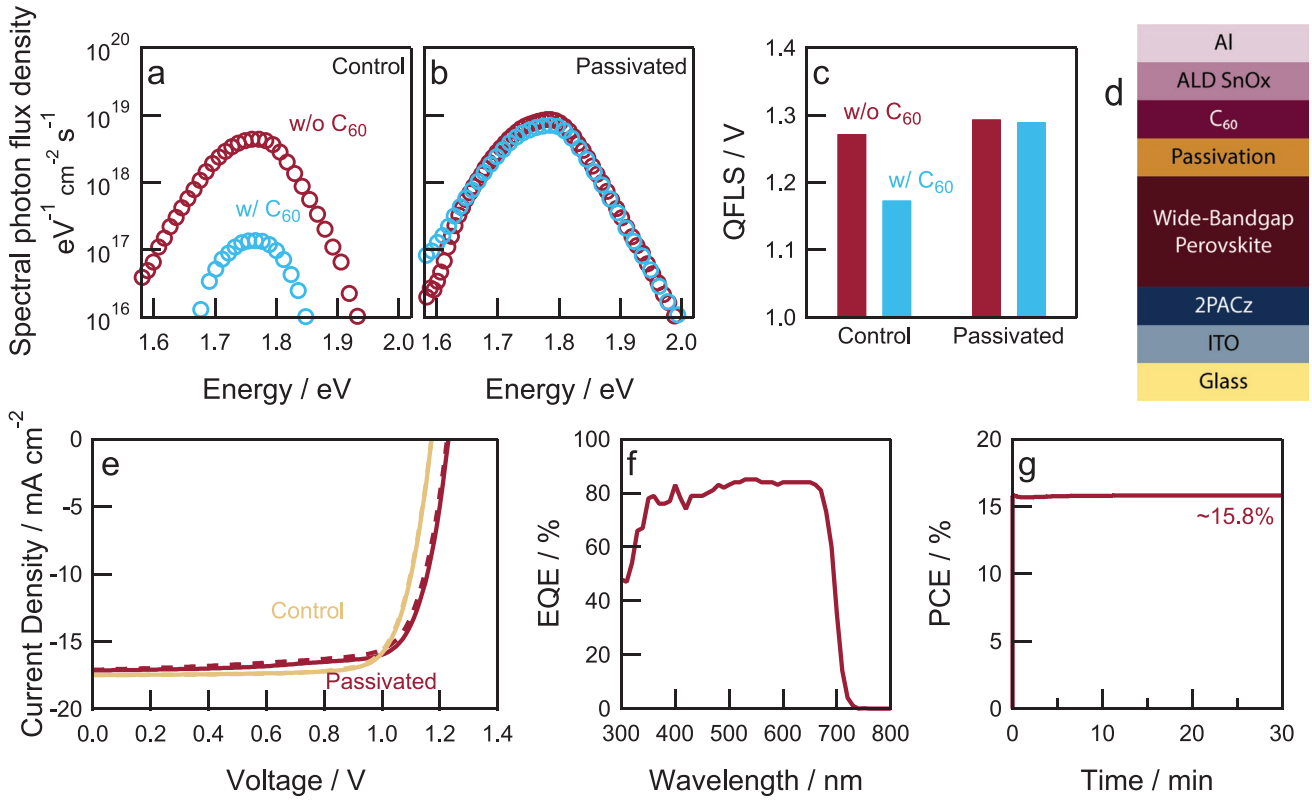

Figure 1. Mixed-halide 1.77 eV wide-bandgap PSC. a) Absolute photoluminescence spectra of perovskite thin films on glass/ITO/2PACz (control) with or without a 20 nm-thick C_{60} overlayer. b) Absolute photoluminescence spectra of choline chloride-passivated perovskite thin films on glass/ITO/2PACz (passivated) with or without a 20 nm-thick C_{60} overlayer. c) QFLS of control and passivated 1.77 eV perovskite thin films without (red bar) or with (blue bar) a 20 nm-thick C_{60} overlayer. d) Device layout of representative planar *p-i-n* 1.77 eV perovskite single-junction solar cell. 2PACz is a thin monolayer (< 5 nm) and choline chloride surface treatment does not result in a measurable change of the perovskite layer thickness. e) Current density versus voltage (*J–V*) characteristics of a single-junction solar cell with an unpassivated (control) or choline chloride-treated (passivated) 1.77 eV perovskite film. Solid and dashed lines represent reverse and forward voltage scans respectively. f) EQE spectrum of passivated solar cell. g) Stabilized maximum power point (MPP) tracking of single-junction solar cell, with choline chloride treatment, at a voltage, V_{MPP} = 1.05 V.

presents significant challenges to experimental yield which could not be overcome with common strategies such as solvent washing of the HTL surface and mechanical spreading of the perovskite precursor.[33]

A mixed Pb—Sn narrow-bandgap perovskite based on $FA_{0.66}MA_{0.34}Pb_{0.5}Sn_{0.5}I_3$ (1.23 eV) was prepared by a two-step solution process, which facilitates a homogeneous transition of mixed Pb- and Sn-based phases.[34] First, an inorganic precursor film containing SnI_2, PbI_2, and SnF_2 was deposited, dried at room temperature, and treated by an interdiffusion of FAI/MAI salts from solution and subsequent thermal annealing to obtain a polycrystalline film. In our initial attempt to compensate for the low absorptivity in the NIR region, perovskite layers with thicknesses ranging from 400 to 800 nm were prepared by changing the precursor solution concentration or spin-coating speed. XRD patterns (Figure S6, Supporting Information) confirm the formation of a cubic phase, whereas a comparable full width at half-maximum (FWHM) value of the strongest (100) peak indicates a similar crystallinity among all perovskite films. In addition, the top-view scanning electron microscopy (SEM) images (Figure S7, Supporting Information) show that all perovskite films are compact and pinhole-free, with slightly enlarged grain sizes with increasing layer thicknesses. Correspondingly, single-junction narrow-bandgap solar cells (**Figure 2**a) exhibit an enhanced NIR spectral response by displaying an external quantum efficiency (EQE)-integrated J_{sc} of 28.4, 29.0, and 29.2 mA cm^{-2} for 430, 600, and 840 nm-thick absorber layers, respectively (Figure 2b and Figure S8, Supporting Information). However, beyond a 600 nm thickness, the J_{sc} increment becomes smaller while both the V_{oc} and FF slightly reduce, which we attribute to limited carrier diffusion lengths in mixed Pb—Sn perovskite films.[16]

In narrow-bandgap PSCs, using ultrathin HTLs helps curtail optical losses in the NIR region without compromising the electrical performance.[35] Using a 600-nm thick perovskite absorber, we compared devices based on PEDOT:PSS at varied thicknesses with a [2-(3,6-dimethoxy-9H-carbazol-9-yl)ethyl]phosphonic acid (MeO-2PACz) SAM as the HTL. The EQE spectra (Figure 2c) suggest an enhanced J_{sc} from 28.8 to 29.0, and 29.8 mA cm^{-2} by reducing the thickness of PEDOT:PSS layers from 50 to 20, and 5 nm, respectively; meanwhile, a MeO-2PACz based device yields a higher J_{sc} of 30.6 mA cm^{-2}. Here, the increased spectral response is mainly attributed to a combined effect of constructive interference and reduced parasitic absorption in devices with thinner HTLs. We note that all the devices yield similar V_{oc}

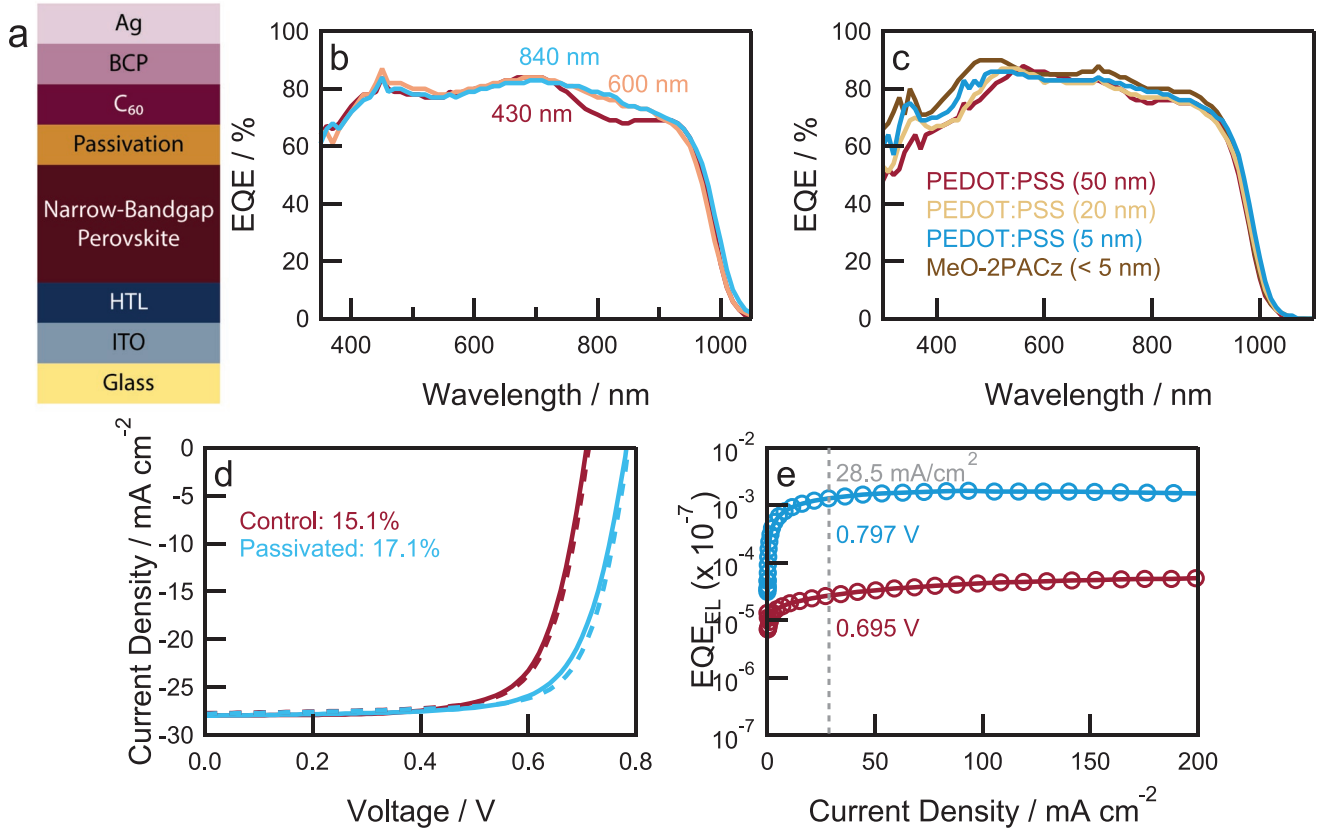

Figure 2. Mixed Pb—Sn 1.23 eV narrow-bandgap PSC. a) Device structure of a representative planar *p-i-n* 1.23 eV single-junction solar cell. b) EQE spectra of PSCs with different thicknesses of narrow-bandgap perovskite absorber layers. c) EQE spectra of PSCs with different HTLs using a 600 nm-thick perovskite film. d) *J–V* characteristics of PSCs with and without CdI_2 passivation at the perovskite/C_{60} interface. Solid and dashed lines represent reverse and forward voltage scans respectively. e) External EL quantum efficiency versus current density for PSCs shown in panel (d).

and FF (Figure S9, Supporting Information), suggesting that the narrow-bandgap devices are not severely limited by the perovskite/HTL interface.

Point defects at the perovskite surface triggered by volatile component loss and ion migration create deep-level trap states and substantial non-radiative recombination losses.[36] In narrow-bandgap PSCs, we found that passivating the perovskite/C_{60} interface with cadmium iodide (CdI_2) effectively increases the V_{oc} from 0.73 to 0.80 V while both the J_{sc} and FF remain intact (Figure 2d and Figure S10, Supporting Information). This corresponds to an enhanced PCE from 15.1% to 17.1% for the interface-passivated device. We note that the post-treatment of a small amount of CdI_2 does not significantly alter the crystallinity, morphology, and energy-level diagram of as-deposited narrow-bandgap perovskite films (Figure S11, Supporting Information). X-ray photoelectron spectroscopy (XPS) confirms the presence of Cd and an increased iodide concentration (Figure S12, Supporting Information) which help suppress atomic vacancies at the perovskite film surface.[37] We further corroborate the efficacy of CdI_2 in reducing the non-radiative recombination losses by performing electroluminescence (EL) external quantum efficiency (EQE_{EL}) measurements (Figure 2e and Figure S13, Supporting Information). For solar cells operated under a forward current density near the J_{sc} (28.5 mA cm^{-2}), we determined a V_{oc} of 0.70 and 0.80 V from the EQE_{EL} for the control and CdI_2-passivated devices, respectively, which are in excellent agreement with the values (0.73 and 0.80 V) measured from the *J–V* characteristics under simulated AM 1.5G illumination.

We conducted optical simulations of integrated all-perovskite tandem solar cells (cell architecture in **Figure 3**a) using the wavelength-dependent refractive indices (*n*) and extinction coefficients (*k*) of all layers (Figure S14, Supporting Information) to identify the origin of optical losses due to reflection or parasitic absorption. Such loss processes are critical in tandem solar cells due to the complex optical environment that can limit absorption in either sub-cell thereby increasing the current-mismatch between them, eventually leading to the current-limiting sub-cell determining the J_{sc} of the tandem. Figure 3b shows the absorptance (*A*) of the layers in the tandem developed on commonly used ITO as the front TCO contact together with the reflectance (*R*) of the device stack. An ICL comprising a stack of C_{60}/spatial atomic layer deposited (sALD) SnO_x/Au/PEDOT:PSS was used as the recombination junction to integrate the sub-cells. Here, a 50 nm-thick PEDOT:PSS layer was used as the hole-transporting layer in the narrow-bandgap sub-cell. It is clear that parasitic absorption causes the narrow-bandgap sub-cell to lose 10–15% absorption in the 700–1000 nm range. The losses stem from free carrier absorption in the ITO layer and absorption in the PEDOT:PSS layer. A small loss

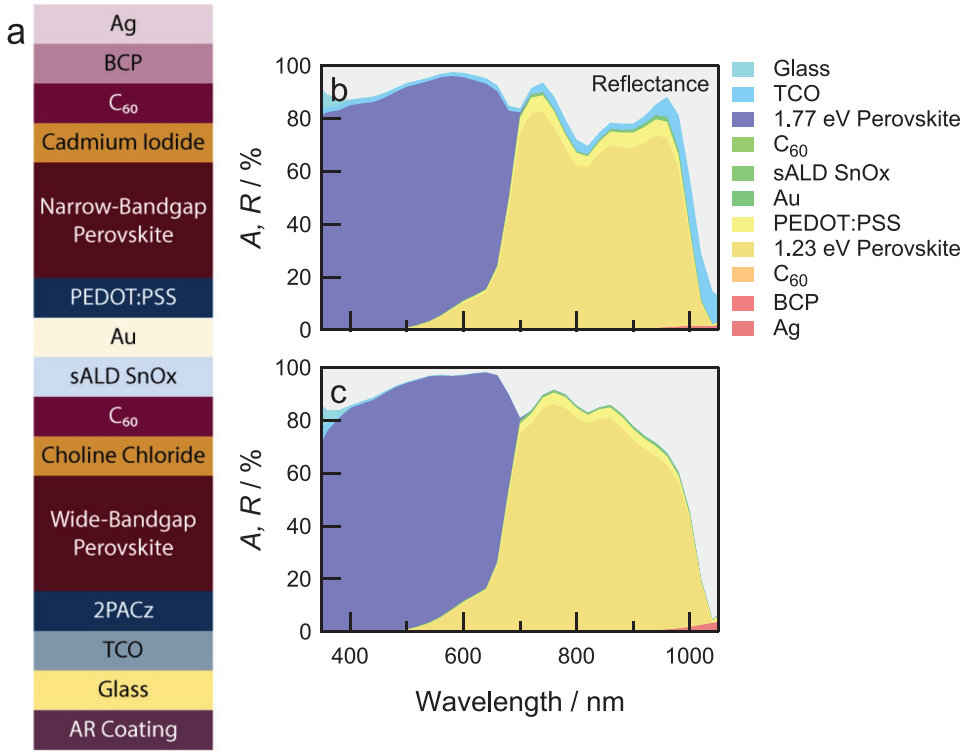

Figure 3. Optical simulation of all-perovskite tandem solar cells. a) Schematic of monolithic all-perovskite tandem solar cell. b) Simulated absorptance (*A*) of all-perovskite tandem solar cells using ITO as TCO and a 50 nm PEDOT:PSS hole-transport layer in the narrow-bandgap sub-cell. c) Same for IOH as TCO and a 20 nm PEDOT:PSS hole-transport layer in the narrow-bandgap sub-cell. The grey shaded areas represent reflectance (*R*) in each case.

contribution also stems from the Au interlayer in the recombination junction.

Hydrogenated indium oxide (IOH) has been used as a transparent contact due to its high transparency (optical constants in Figure S14, Supporting Information) which makes it ideal for use in multijunction devices limited by the free-carrier absorption of ITO.[38,39] Furthermore, as described before, the use of a 20 nm-thick PEDOT:PSS layer can increase light absorption in the narrow-bandgap solar cell. Figure 3c shows the absorption contributions in tandem cells using IOH instead of ITO and a thinner (20 nm-thick) PEDOT:PSS layer. It is clear that the loss due to parasitic absorption is now reduced to ≈5% in the 700–1000 nm range, dominated by absorption in the PEDOT:PSS layer (Figures S15 and S16, Supporting Information). The minor contribution of the Au interlayer can also be reduced by using a thin (5 nm) ITO layer instead. The loss due to the hole-transport layer for the narrow-bandgap sub-cell can be further reduced by using a SAM (MeO-2PACz) which is optically more transparent due to its low thickness (Figure S17, Supporting Information). Due to their surface binding mechanism, however, spin-coating SAMs based on phosphonic acid anchoring groups requires the use of metal oxide layers, such as an ITO surface, at the recombination junction.

Monolithic all-perovskite tandem solar cells were prepared using the 1.77 and 1.23 eV sub-cells, connected through a C_{60}/sALD SnO_x/Au/PEDOT:PSS recombination junction.[25] Motivated by favorable optical simulations, a highly transparent IOH front contact was used and compared to an ITO transparent electrode. Surface morphology and XRD patterns indicate that the 1.77 eV-perovskite film is comparable irrespective of the TCO layer (Figure S18, Supporting Information). As a consequence, the PV performance of a single-junction cell is largely unaffected by replacing the front ITO contact with the IOH layer. Nevertheless, in tandem, along with the use of a thin HTL material in the 1.23 eV sub-cell, the improved light management allows for a higher response in the 1.23 eV sub-cell which reduces the current-mismatch between the two sub-cells. As a result, the J_{sc} in the tandem can be increased (**Figure 4**a) due to the higher EQE in the 1.23 eV sub-cell (Figure 4b). Here, when developed on an ITO front contact, a current mismatch of ≈2.2 mA cm^{-2} limits the J_{sc} of the tandem to ≈13.8 mA cm^{-2}. However, upon using an IOH front electrode instead, the mismatch decreases to ≈1.0 mA cm^{-2}, increasing the tandem J_{sc} to > 15.2 mA cm^{-2}. The EQE of the 1.23 eV sub-cell in the tandem can be further increased by replacing the thin Au layer with a 5 nm thick sputtered ITO interlayer (Figure S19, Supporting Information). In that case, the 1.23 eV sub-cell ceases to be the limiting cell with the mismatch reduced to ≈0.2 mA cm^{-2}. As a result, the tandem yields a high J_{sc} of ≈16.3 mA cm^{-2} using only a 600 nm-thick 1.23 eV perovskite absorber, further emphasizing the value in light management strategies as a route to increasing PV performance. However, the lower conductivity of ITO compared to Au leads to a loss in the V_{oc} which effectively decreases device performance (Figure S20, Supporting Information).

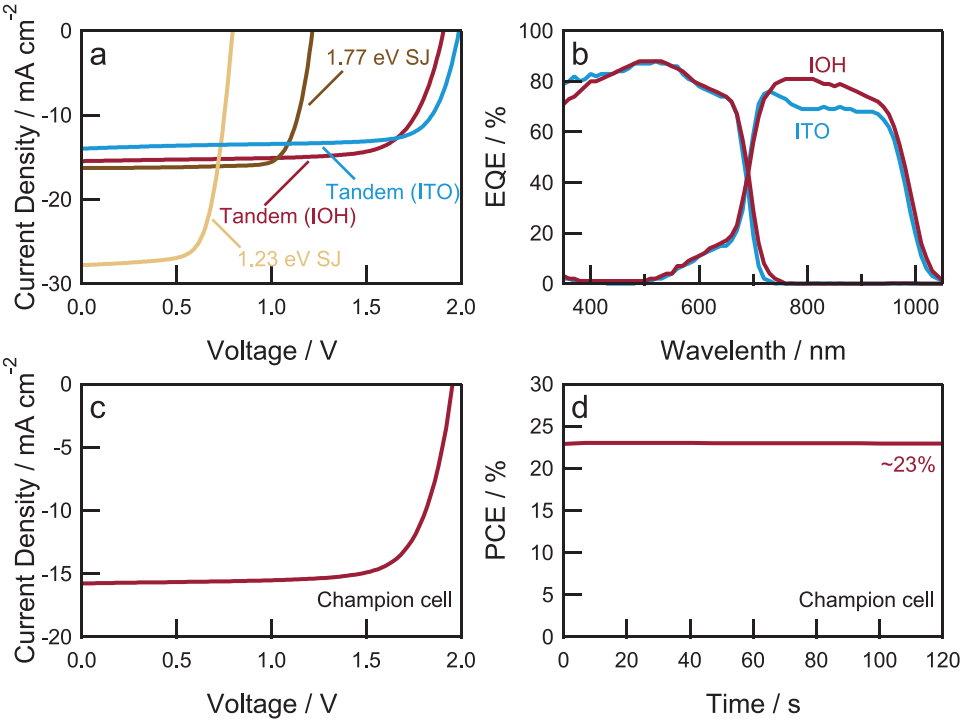

Figure 4. Monolithic all-perovskite tandem solar cells. a) *J–V* characteristics of tandem-compatible 1.23 eV and 1.77 eV single-junction, and monolithic tandem solar cells developed on ITO or IOH front electrodes using 20 nm-thick PEDOT:PSS layers in the narrow-bandgap sub-cell. b) EQE contributions of individual sub-cells in monolithic tandem solar cells developed on ITO or IOH front electrodes. c) *J–V* characteristics of champion tandem solar cell developed on IOH front electrode. d) MPP tracking measurement of the champion tandem solar cell.

The use of an ITO interlayer in the recombination junction also allows the application of SAM hole-transporting materials.[12] However, unlike PEDOT:PSS, MeO-2PACz does not planarize the underlying 1.77 eV perovskite sub-cell surface,[24] thereby providing a rough substrate for the 1.23 eV perovskite to be processed on. Consequently, the spread in PV performance is found to be larger when using MeO-2PACz at the hole-transporting interface of the 1.23 eV sub-cell (Figure S21, Supporting Information).

Based on these optimization strategies to minimize non-radiative recombination in sub-cells and reduce optical losses in the tandem, a champion device (Figure 4c,d, **Table 1**) demonstrating a PCE of ≈23.1% can be developed (solar simulator spectrum in Figure S22, Supporting Information). A high V_{oc} of ≈1.95 V represents a small voltage loss of ≈50 mV at the recombination junction compared to the summed V_{oc} of the sub-cells.

3. Conclusions

We report the development of a >23% efficient monolithic all-perovskite tandem solar cell enabled by 1.77 and 1.23 eV sub-cells with high radiative yield. The low non-radiative recombination is achieved by surface passivation of perovskite films in post-treatment steps that consequently increase the V_{oc} of single-junction solar cells. Upon integration in tandem, this high radiative yield translates to a high V_{oc} further aided by a low-loss recombination junction. The tandem performance

Table 1. Photovoltaic parameters of single-junction and tandem PSCs based on IOH front electrode.

Devices	J_{sc} [mA cm^{-2}]	V_{oc} [V]	FF	PCE[a)] [%]	J_{sc}[b)] [mA cm^{-2}]	PCE[c)] [%]
1.77 eV	17.1	1.23	0.76	16.0	17.0	15.9
	16.6 ± 0.3	1.24 ± 0.01	0.78 ± 0.01	16.1 ± 0.3[d)]		
1.23 eV	28.0	0.80	0.76	17.1	28.9	17.6
	28.2 ± 0.8	0.79 ± 0.02	0.74 ± 0.02	16.5 ± 0.6[d)]		
Tandem	15.8	1.95	0.75	23.1		
	15.5 ± 0.2	1.93 ± 0.02	0.73 ± 0.02	21.9 ± 0.5[d)]		

[a)]The data was extracted from stabilized *J–V* curves under simulated AM 1.5G illumination (100 mW cm^{-2}). The aperture area was 6.76 mm^2 for single-junction devices and 9.00 mm^2 for tandem devices; [b)]Calculated by integrating the EQE spectrum with the AM1.5G spectrum; [c)]Corrected PCE obtained by calculating the J_{sc} integrated from EQE spectrum and V_{oc} and FF from the *J–V* measurement; [d)]Averaged PV parameters taken from at least 15 devices.

is improved significantly by using an optically benign front transparent electrode (IOH) to replace ITO which typically restricts the NIR response of the tandem. Furthermore, by reducing optical losses occurring at the recombination junction, either through the Au interlayer or due to the typically thick PEDOT:PSS hole transport contact, the EQE response in the 1.23 eV sub-cell can be increased, leading to a high current-matched J_{sc} in the tandem. Compared to single-junction devices, the tandem represents an efficiency increase of ≈7 (wide-bandgap) and ≈6% (narrow-bandgap) percentage points. Taken together, these results emphasize the role of interfacial passivation in improving the V_{oc} in multijunction PV devices. Moreover, we clearly show that the optical response of such solar cells can heavily influence the performance of devices and can be tuned through simple light management strategies aided by accurate optical simulations.

Supporting Information

Supporting Information is available from the Wiley Online Library or from the author.

Acknowledgements

K.D. and J.W. contributed equally to this work. The authors acknowledge the Netherlands Organization for Scientific Research (NWO) for funding through the Joint Solar Programme III (Project 680.91.011) and the NWO Spinoza grant. The authors further acknowledge funding from the Ministry of Education, Culture, and Science (Gravity program 024.001.035). The authors thank Tom van der Pol for ellipsometry measurements on some of the layers used in the multijunction devices.

Conflict of Interest

The authors declare no conflict of interest.

Data Availability Statement

The data that support the findings of this study are available from the corresponding author upon reasonable request.

Keywords

metal-halide perovskites, optical modeling, passivation, tandem solar cells

Received: December 9, 2021
Published online:

[1] J. F. Geisz, R. M. France, K. L. Schulte, M. A. Steiner, A. G. Norman, H. L. Guthrey, M. R. Young, T. Song, T. Moriarty, *Nat. Energy* **2020**, *5*, 326.
[2] R. Wang, T. Huang, J. Xue, J. Tong, K. Zhu, Y. Yang, *Nat. Photonics* **2021**, *15*, 411.
[3] M. A. Green, E. D. Dunlop, J. Hohl-Ebinger, M. Yoshita, N. Kopidakis, X. Hao, *Prog. Photovolt.: Res. Appl.* **2021**, *29*, 657.
[4] M. Jošt, L. Kegelmann, L. Korte, S. Albrecht, *Adv. Energy Mater.* **2020**, *10*, 1904102.
[5] J. Xu, C. C. Boyd, Z. J. Yu, A. F. Palmstrom, D. J. Witter, B. W. Larson, R. M. France, J. Werner, S. P. Harvey, E. J. Wolf, W. Weigand, S. Manzoor, M. van Hest, J. J. Berry, J. M. Luther, Z. C. Holman, M. D. McGehee, *Science* **2020**, *367*, 1097.
[6] F. Hao, C. C. Stoumpos, R. P. Chang, M. G. Kanatzidis, *J. Am. Chem. Soc.* **2014**, *136*, 8094.
[7] T. Moot, J. Werner, G. E. Eperon, K. Zhu, J. J. Berry, M. D. McGehee, J. M. Luther, *Adv. Mater.* **2020**, *32*, 2003312.
[8] S. Mahesh, J. M. Ball, R. D. J. Oliver, D. P. McMeekin, P. K. Nayak, M. B. Johnston, H. J. Snaith, *Energy Environ. Sci.* **2020**, *13*, 258.
[9] M. Stolterfoht, P. Caprioglio, C. M. Wolff, J. A. Márquez, J. Nordmann, S. Zhang, D. Rothhardt, U. Hörmann, Y. Amir, A. Redinger, L. Kegelmann, F. Zu, S. Albrecht, N. Koch, T. Kirchartz, M. Saliba, T. Unold, D. Neher, *Energy Environ. Sci.* **2019**, *12*, 2778.
[10] K. Datta, B. T. van Gorkom, Z. Chen, M. J. Dyson, T. P. A. van der Pol, S. C. J. Meskers, S. Tao, P. A. Bobbert, M. M. Wienk, R. A. J. Janssen, *ACS Appl. Energy Mater.* **2021**, *4*, 6650.
[11] M. Abdi-Jalebi, Z. Andaji-Garmaroudi, S. Cacovich, C. Stavrakas, B. Philippe, J. M. Richter, M. Alsari, E. P. Booker, E. M. Hutter, A. J. Pearson, S. Lilliu, T. J. Savenije, H. Rensmo, G. Divitini, C. Ducati, R. H. Friend, S. D. Stranks, *Nature* **2018**, *555*, 497.
[12] A. Al-Ashouri, A. Magomedov, M. Roß, M. Jošt, M. Talaikis, G. Chistiakova, T. Bertram, J. A. Márquez, E. Köhnen, E. Kasparavičius, S. Levcenco, L. Gil-Escrig, C. J. Hages, R. Schlatmann, B. Rech, T. Malinauskas, T. Unold, C. A. Kaufmann, L. Korte, G. Niaura, V. Getautis, S. Albrecht, *Energy Environ. Sci.* **2019**, *12*, 3356.
[13] S. Gharibzadeh, B. Abdollahi Nejand, M. Jakoby, T. Abzieher, D. Hauschild, S. Moghadamzadeh, J. A. Schwenzer, P. Brenner, R. Schmager, A. A. Haghighirad, L. Weinhardt, U. Lemmer, B. S. Richards, I. A. Howard, U. W. Paetzold, *Adv. Energy Mater.* **2019**, *9*, 1803699.
[14] J. Thiesbrummel, V. M. Le Corre, F. Peña-Camargo, L. Perdigón-Toro, F. Lang, F. Yang, M. Grischek, E. Gutierrez-Partida, J. Warby, M. D. Farrar, S. Mahesh, P. Caprioglio, S. Albrecht, D. Neher, H. J. Snaith, M. Stolterfoht, *Adv. Energy Mater.* **2021**, *11*, 2101447.
[15] Z. Yang, Z. Yu, H. Wei, X. Xiao, Z. Ni, B. Chen, Y. Deng, S. N. Habisreutinger, X. Chen, K. Wang, J. Zhao, P. N. Rudd, J. J. Berry, M. C. Beard, J. Huang, *Nat. Commun.* **2019**, *10*, 4498.
[16] R. Lin, K. Xiao, Z. Qin, Q. Han, C. Zhang, M. Wei, M. I. Saidaminov, Y. Gao, J. Xu, M. Xiao, A. Li, J. Zhu, E. H. Sargent, H. Tan, *Nat. Energy* **2019**, *4*, 864.
[17] K. Xiao, R. Lin, Q. Han, Y. Hou, Z. Qin, H. T. Nguyen, J. Wen, M. Wei, V. Yeddu, M. I. Saidaminov, Y. Gao, X. Luo, Y. Wang, H. Gao, C. Zhang, J. Xu, J. Zhu, E. H. Sargent, H. Tan, *Nat. Energy* **2020**, *5*, 870.
[18] J. Tong, Z. Song, D. H. Kim, X. Chen, C. Chen, A. F. Palmstrom, P. F. Ndione, M. O. Reese, S. P. Dunfield, O. G. Reid, J. Liu, F. Zhang, S. P. Harvey, Z. Li, S. T. Christensen, G. Teeter, D. Zhao, M. M. Al-Jassim, M. van Hest, M. C. Beard, S. E. Shaheen, J. J. Berry, Y. Yan, K. Zhu, *Science* **2019**, *364*, 475.
[19] D. Zhao, C. Chen, C. Wang, M. M. Junda, Z. Song, C. R. Grice, Y. Yu, C. Li, B. Subedi, N. J. Podraza, X. Zhao, G. Fang, R.-G. Xiong, K. Zhu, Y. Yan, *Nat. Energy* **2018**, *3*, 1093.
[20] G. Kapil, T. Bessho, T. Maekawa, A. K. Baranwal, Y. Zhang, M. A. Kamarudin, D. Hirotani, Q. Shen, H. Segawa, S. Hayase, *Adv. Energy Mater.* **2021**, *11*, 2101069.
[21] R. K. Kothandaraman, Y. Jiang, T. Feurer, A. N. Tiwari, F. Fu, *Small Methods* **2020**, *4*, 2000395.
[22] Z. Yu, Z. Yang, Z. Ni, Y. Shao, B. Chen, Y. Lin, H. Wei, Z. J. Yu, Z. Holman, J. Huang, *Nat. Energy* **2020**, *5*, 657.
[23] A. F. Palmstrom, G. E. Eperon, T. Leijtens, R. Prasanna, S. N. Habisreutinger, W. Nemeth, E. A. Gaulding, S. P. Dunfield,

M. Reese, S. Nanayakkara, T. Moot, J. Werner, J. Liu, B. To, S. T. Christensen, M. D. McGehee, M. F. A. M. van Hest, J. M. Luther, J. J. Berry, D. T. Moore, *Joule* **2019**, *3*, 2193.

[24] K. Xiao, J. Wen, Q. Han, R. Lin, Y. Gao, S. Gu, Y. Zang, Y. Nie, J. Zhu, J. Xu, H. Tan, *ACS Energy Lett.* **2020**, *5*, 2819.

[25] J. Wang, V. Zardetto, K. Datta, D. Zhang, M. M. Wienk, R. A. J. Janssen, *Nat. Commun.* **2020**, *11*, 5254.

[26] M. Jošt, E. Köhnen, A. B. Morales-Vilches, B. Lipovšek, K. Jäger, B. Macco, A. Al-Ashouri, J. Krč, L. Korte, B. Rech, R. Schlatmann, M. Topič, B. Stannowski, S. Albrecht, *Energy Environ. Sci.* **2018**, *11*, 3511.

[27] E. Aydin, M. De Bastiani, X. Yang, M. Sajjad, F. Aljamaan, Y. Smirnov, M. N. Hedhili, W. Liu, T. G. Allen, L. Xu, E. Van Kerschaver, M. Morales-Masis, U. Schwingenschlögl, S. De Wolf, *Adv. Funct. Mater.* **2019**, *29*, 1901741.

[28] M. T. Hörantner, T. Leijtens, M. E. Ziffer, G. E. Eperon, M. G. Christoforo, M. D. McGehee, H. J. Snaith, *ACS Energy Lett.* **2017**, *2*, 2506.

[29] I. L. Braly, D. W. deQuilettes, L. M. Pazos-Outón, S. Burke, M. E. Ziffer, D. S. Ginger, H. W. Hillhouse, *Nat. Photonics* **2018**, *12*, 355.

[30] X. Zheng, B. Chen, J. Dai, Y. Fang, Y. Bai, Y. Lin, H. Wei, X. C. Zeng, J. Huang, *Nat. Energy* **2017**, *2*, 17102.

[31] A. Al-Ashouri, E. Kohnen, B. Li, A. Magomedov, H. Hempel, P. Caprioglio, J. A. Marquez, A. B. Morales Vilches, E. Kasparavicius, J. A. Smith, N. Phung, D. Menzel, M. Grischek, L. Kegelmann, D. Skroblin, C. Gollwitzer, T. Malinauskas, M. Jost, G. Matic, B. Rech, R. Schlatmann, M. Topic, L. Korte, A. Abate, B. Stannowski, D. Neher, M. Stolterfoht, T. Unold, V. Getautis, S. Albrecht, *Science* **2020**, *370*, 1300.

[32] I. Levine, A. Al-Ashouri, A. Musiienko, H. Hempel, A. Magomedov, A. Drevilkauskaite, V. Getautis, D. Menzel, K. Hinrichs, T. Unold, S. Albrecht, T. Dittrich, *Joule* **2021**, *5*, 2915.

[33] E. Gutierrez-Partida, H. Hempel, S. Caicedo-Dávila, M. Raoufi, F. Peña-Camargo, M. Grischek, R. Gunder, J. Diekmann, P. Caprioglio, K. O. Brinkmann, H. Köbler, S. Albrecht, T. Riedl, A. Abate, D. Abou-Ras, T. Unold, D. Neher, M. Stolterfoht, *ACS Energy Lett.* **2021**, *6*, 1045.

[34] J. Wang, K. Datta, J. Li, M. A. Verheijen, D. Zhang, M. M. Wienk, R. A. J. Janssen, *Adv. Energy Mater.* **2020**, *10*, 2000566.

[35] P. Gómez, J. Wang, M. Más-Montoya, D. Bautista, C. H. L. Weijtens, D. Curiel, R. A. J. Janssen, *Sol. RRL* **2021**, *5*, 2100454.

[36] J. Ye, M. M. Byranvand, C. O. Martinez, R. L. Z. Hoye, M. Saliba, L. Polavarapu, *Angew. Chem., Int. Ed.* **2021**, *60*, 21636.

[37] M. I. Saidaminov, J. Kim, A. Jain, R. Quintero-Bermudez, H. Tan, G. Long, F. Tan, A. Johnston, Y. Zhao, O. Voznyy, E. H. Sargent, *Nat. Energy* **2018**, *3*, 648.

[38] S. Moghadamzadeh, I. M. Hossain, M. Loy, D. B. Ritzer, H. Hu, D. Hauschild, A. Mertens, J. P. Becker, A. A. Haghighirad, E. Ahlswede, L. Weinhardt, U. Lemmer, B. A. Nejand, U. W. Paetzold, *ACS Appl. Mater. Interfaces* **2021**, *13*, 46488.

[39] Y. Jiang, T. Feurer, R. Carron, G. T. Sevilla, T. Moser, S. Pisoni, R. Erni, M. D. Rossell, M. Ochoa, R. Hertwig, A. N. Tiwari, F. Fu, *ACS Nano* **2020**, *14*, 7502.